Science

AAAS

Supplementary Materials for

Magma accumulation at depths of prior rhyolite storage beneath Yellowstone Caldera

Ross Maguire *et al*.

Corresponding author: Ross Maguire, rossrm@illinois.edu

The PDF file includes:

Materials and Methods
Figs. S1 to S11
Tables S1 and S2
References

Materials and Methods

<u>Ambient</u> <u>Noise</u> <u>Correlation</u>

In this study we utilized continuous recordings of ground motion from all available broadband seismic stations deployed in our study region between 2000-2018, which included a total of 232 stations (Table S1). The data were downloaded from the Incorporated Research Institution for Seismology (IRIS) Data Management Center using the ObsPy FDSN web service client (*32*). To calculate ambient noise correlation functions (NCFs), we selected 3 time periods when simultaneous network deployments enabled dense interstation path coverage of the Yellowstone region. The first time period (from 2000-03-01 to 2001-08-10) predominantly consisted of stations from the Geodynamics of the Yellowstone Hotspot from Seismic and GPS imaging Experiment (XC) and the Montana BB Array (XS), which temporally overlapped for approximately one month. The second time period (from 2007-01-01 to 2010-12-31) included the Earthscope/USArray Transportable Array deployment (TA), the Bighorn Arch Seismic Experiment (XV), and the Noise Observatory for Imaging the Subsurface beneath Yellowstone (Z2; *33*). The last period (from 2017-01-01 to 2018-01-01) was chosen to include 15 stations from the Yellowstone National Park Seismograph Network (WY) that were upgraded from short period to broadband instruments. During all time periods, stations from permanent networks IW (Intermountain West Seismic Network) and US (United States National Seismic Network) were included in the cross correlations, when available.

Vertical component NCFs between all interstation pairs were calculated closely following the methodology of Bensen et al., (2007) (*34*). First, daily vertical component waveforms were corrected for instrument response and resampled to 2 Hz. Next, waveforms were temporally normalized using a running average filter of 64 s and spectrally whitened. These steps are performed to minimize the influence of transient signals (e.g., from earthquakes), and to remove the bias from peaks in the ambient noise spectrum, typically near 15 s and 7.5 s (i.e., the primary and secondary microseisms). After pre-processing, daily data were trimmed into 12 overlapping 4-hour segments, and each segment was cross correlated and stacked to produce a daily correlation function. This process was repeated for all days, and daily correlation functions were linearly stacked to produce the final NCF.

<u>Traditional</u> <u>Ambient</u> <u>Noise</u> <u>Tomography</u>

To construct a starting model for full waveform inversion (FWI) we used our dataset to create a 3D V_S model using traditional ambient noise tomography (ANT) (*35, 36*), which is based on inverting Rayleigh wave group or phase velocity dispersion measurements extracted from NCFs. Here, we measured phase velocity dispersion curves for periods between 6 – 30 s for all interstation pairs using automated frequency time analysis (FTAN). Phase velocity measurements for a given period were accepted if the signal-to-noise ratio (SNR) was greater than 10 and the interstation distance was greater than 2 seismic wavelengths. The culled dataset was used to invert for phase velocity maps at all observed periods using 2D Voronoi tomography (*37*). Following this approach, we parameterize each map using 300 randomly located Voronoi cells and solve the linearized tomography problem a total of 100 times to create an ensemble of solutions, where each solution uses a different realization of the random Voronoi projection. All solutions are mapped onto an underlying fine-scale grid on which the mean and standard deviation of the model ensemble are computed (Fig. S1). The forward problem (i.e., calculation

of ray paths and travel times) is computed by numerically solving the Eikonal equation using the Python-based software package PyKonal (*38*).

Finally, the 3D V$_S$ model is obtained by inverting local 1D dispersion curves at all model points on a 0.1 x 0.1 degree grid using a Markov chain Monte Carlo (McMC) approach (*15*). In each 1D inversion, the model is parameterized using 5 B-spline functions in the crust, and a single layer in the mantle. Because surface wave dispersion measurements are not strongly sensitive to the Moho depth (i.e., the Moho depth trades off strongly with the seismic velocities above and below the boundary), we include an *a priori* estimate of the crustal thickness from Schmandt et al., (2015) (*39*), which is constrained by a combination of receiver function imaging and Rayleigh wave phase velocity and ellipticity measurements. In our inversion, the Moho depth is assigned an uncertainty of +/- 3 km from the depth constraint from Schmandt et al. (2015). In the McMC search, proposed models are firstly randomly selected from a uniform prior distribution to form each Markov chain. Then, the models are randomly sampled from a Gaussian prior distribution within the Markov chain, which contains 2500 iterations before a new chain is initiated by randomly sampling the model space again. The model selection during the McMC search is guided by the Metropolis-Hasting algorithm (*40*). The predicted dispersion curve is calculated using the Computer Programs in Seismology software package (*41*). The probability of acceptance of a proposed model **m** is defined by the likelihood function

$$P \ = \ \exp\left(\frac{-\varphi(m)}{2}\right)$$

where φ is the misfit between the observed and predicted phase travel times

$$\varphi(m) \ = \ \frac{\left(T_{obs} - T(m)\right)^2}{\sigma^2}$$

The data uncertainties σ, for each local dispersion curve are inherited from the 2D Voronoi tomography. At each grid point, the final 1D V$_S$ model is selected as the average of the 2000 best fitting models from the Markov chain.

Full waveform inversion
In full waveform inversion (FWI), the starting wave speed model (here, the V$_S$ model calculated using traditional ANT) is iteratively updated based on the calculation of the gradient of the misfit function with respect to the model parameters (i.e., sensitivity kernel) via the adjoint method (*42*). The computation of the sensitivity kernels requires one forward wavefield simulation and one adjoint wavefield simulation per seismic source. The interaction of the forward wavefield (i.e., the wavefield emanating from a virtual source) and the adjoint wavefield (i.e., the back-propagating wavefield from all adjoint sources) creates the sensitivity kernel (*19,43*).

At each iteration, we select a subset of all virtual sources to be used in the adjoint inversion. For iterations 1 – 5 we select virtual sources from the TA, WY, IW, and US networks for a total of 90 virtual sources. For iterations 6 – 10, we start to include the XC and XS networks as virtual

sources (167 total sources). Virtual sources from networks Z2 and XV are left out of the adjoint inversion but serve as a validation dataset for the final model. Rayleigh wave cross correlation travel time delays are minimized in 6 overlapping period bands (5 - 7 s, 6 - 9 s, 8 - 12 s, 10 - 16 s, 15 - 23 s, 20 - 30 s) at each iteration according to the misfit function

$$\chi = \frac{1}{N}\sum_{i=1}^{N}\frac{1}{2}\sum_{j=1}^{M}\Delta T_j^2$$

where χ is the misfit, N is the number of period bands, M is the number of measurements in each period band, and ΔT_j is the cross-correlation travel time delay for the j-th measurement. Once the kernels are calculated for all virtual sources, we sum them and apply smoothing using a Gaussian filter with a length scale of 10 km in the horizontal direction and 1 km in the vertical direction. The smoothed kernel is then preconditioned using the inverse of the Hessian matrix, yielding the final Fréchet kernel **K** which is used to update the current model. **K** defines the step direction to update the model but the step size α that yields the largest misfit reduction needs to be determined to find the optimum model perturbation. Here, we find α using a line search, in which 4 trial step sizes are used to forward predict the wavefield for a subset of 15 events. The step size with the smallest misfit is then chosen to update the model following

m$_{i+1}$ = **m**$_i$ + α **K**

where **m**$_{i+1}$ and **m**$_i$ are the updated are previous models, respectively. Fig. S2 shows the evolution of the misfit over the course of the inversion.

The forward and adjoint wavefield modeling required for the calculation of the adjoint kernels was performed using the spectral-element based code SPECFEM3D Cartesian (*44*). Our model domain spans from –115.5º to -104.0º in longitude, 40.5º to 48.0º in latitude, and extends to a depth of 150 km. The geographic coordinates are projected into the UTM system and the model accommodates surface topography (https://www.gmrt.org/GMRTMapTool/). The numerical mesh is divided into 128 elements in each horizontal dimension and 20 elements in the depth dimension. At a depth of 60 km a doubling layer is introduced to reduce the total number of elements. The maximum time step used in each simulation is 0.05 s and the minimum resolved period is 4.7 s. The starting model is constructed from the traditional ANT model by interpolating the wave speed on all Gauss-Lobatto-Legendre (GLL) grid points of the numerical mesh in the region where the model is defined. Outside of this region, either the horizontally averaged velocity of the ANT model is used, or, at depths below 60 km, the 1D model of the Yellowstone region from Huang et al., (2015) is used. The compressional wave speed V_P and density ρ are scaled from V_S assuming $V_P = 1.73V_S$ and $\rho = 0.72V_S$ (*45*).

To ensure waveforms are robust for fitting, we enforce stricter data selection criteria compared with the data used in the traditional ANT inversion. The data selection process for FWI consists of two stages. First, the SNR of the folded noise correlation function (i.e., the average signal over positive and negative lag times) must be larger than 20, where the noise amplitude is calculated by taking the RMS of the data in a 300 s window following the Rayleigh wave arrival. Second,

the positive and negative lag signals must have a correlation coefficient > 0.5, which helps remove strongly asymmetric noise correlations. Prior to calculating the correlation coefficient a 60-s wide cosine taper centered on the Rayleigh wave is applied (Fig. S3). The accepted NCFs are used to calculate the empirical Green's functions (EGFs) by taking the negative time derivative (46), and the EGFs are compared to synthetic displacement Green's functions to calculate the misfit.

Fig. S4 shows longitudinal slices of model $\mathbf{m_{10}}$ at latitudes ranging between 43.2° - 45.2° and Fig. S5 shows a comparison of the initial model $\mathbf{m_{00}}$ and the final model $\mathbf{m_{10}}$ at depths of 5, 10, 15, and 20 km, and Relative velocity perturbations of model $\mathbf{m_{10}}$ are shown in Figs S6 and S7. Additional waveform fits beyond those in the Main Text are shown in Figs S8 – S10.

Resolution Test
To test how well the low velocity anomaly below Yellowstone caldera is resolved we inverted a synthetic dataset calculated from 3D waveform simulations of a hypothetical magma reservoir using the same approach that was used to invert the observed data. The target model consists of an ellipsoidal anomaly centered below Yellowstone caldera extending to a depth of ~20 km. The strongest velocity anomaly lies in the depth range of approximately 4 – 10 km, with $V_S < 2.0$ km/s (Fig. S11A and C). Using this target model, SPECFEM3D synthetics were calculated by placing vertical point sources at all virtual source locations, allowing us to replicate the source-receiver geometry used in the inversion of the observed data. The starting model for the full waveform inversion was a strongly diminished (peak V_S anomaly of –10%), low pass filtered version of the target model. The inversion of the synthetic data also used a two-stage approach, in which 90 sources were used in iterations 1 – 5, and 167 sources were used in iterations 6 – 10. The recovered model (Fig. S11B and D) almost fully captures the true amplitude and horizontal extent of the target model, suggesting that the main features of the low velocity anomaly below Yellowstone caldera are well resolved. Although the depth extent of the anomaly in the target model does not exceed ~20 km, the recovered model is vertically smeared with a weak low velocity anomaly extending to 40 km depth. Thus, using this approach, a separate, weaker low velocity anomaly associated with a deeper magma reservoir below Yellowstone caldera may be difficult to resolve with surface waves.

Melt fraction modeling
We model the relationship between V_S and melt fraction using the effective-medium theory (24), which enables the calculation of the bulk modulus K and shear modulus μ of a two-phase aggregate of crystals and melt. To calculate V_S of the solid phase, we used the Perplex software to compute K, μ and density ρ for a granitoid at 800°C and 100 MPa. Assuming a lower temperature consistent with cold storage (e.g., 600 – 750 °C) would slightly increase the modeled melt fraction (< 2% difference). Table S2 shows the assumed composition in terms of its major oxide components. If the composition of the solid fraction of the melt reservoir is less silicic (e.g., dacitic) the estimated melt fraction would be slightly higher because the V_S of the solid fraction would increase, and thus more melt would be required to reach the low V_S observed in the reservoir. For the melt phase, we assumed a density of 2.2 kg/m^3 and a bulk modulus of 9.0 GPa (47,48). For simplicity, we neglect the presence of volatiles, although the

presence of H_2O and CO_2 could reduce V_S. To calculate V_S we first compute the velocity of a two-phase aggregate assuming air-filled pore-spaces, and correct the velocity by substituting in the liquid phase following Gassmann's equation (*49*). This calculation yields the low frequency (relaxed) seismic velocity of the partially molten aggregate. To perform these calculations, we used the ElasticC software package available at http://github.com/michpaulatto/ElasticC.

In this approximation, a key parameter is the aspect ratio of the ellipsoidal pore spaces (*24*), which we vary from 0.05 to 1.0. Aspect ratios in the range between 0.1 – 0.15 represent texturally equilibrated partially molten rocks with dihedral angles between $20^o – 40^o$ (*27*). Smaller aspect ratios imply less melt is required to wet grain boundaries compared to more equant pockets isolated near grain boundary junctions. In real systems, melt may be stored both along grain boundaries and in melt-rich lenses or pockets under non-equilibrium conditions, which makes it challenging to ascribe a single aspect ratio for the composite system. In the case of Yellowstone's silicic reservoir, the assumption of textural equilibrium may be reasonable since the system has not erupted in > 70 kyr, although the presence of strong radial anisotropy (*15*) may indicate melt storage in horizontally layered sill complexes. Without knowing the crystal fraction and melt inclusion geometry of such a horizontally layered system an appropriate aspect ratio cannot be determined.

To estimate the volume of silicic melt present in the mid-to-upper crustal reservoir we use the 2.5 km/s velocity contour as a diagnostic of the presence of partial melt. At 5-km this contour corresponds to a melt fraction of >10 %, thus our estimate is a conservative one. The total volume of the reservoir under this assumption is ~11,000 km^3. Although the minimum velocity in the reservoir of ~2.1 km/s corresponds to between 16 – 20 % melt, the melt fraction within the volume would be lower on average. Assuming an average melt fraction in the range of 15% melt implies a total volume of silicic melt of 1,650 km^3.
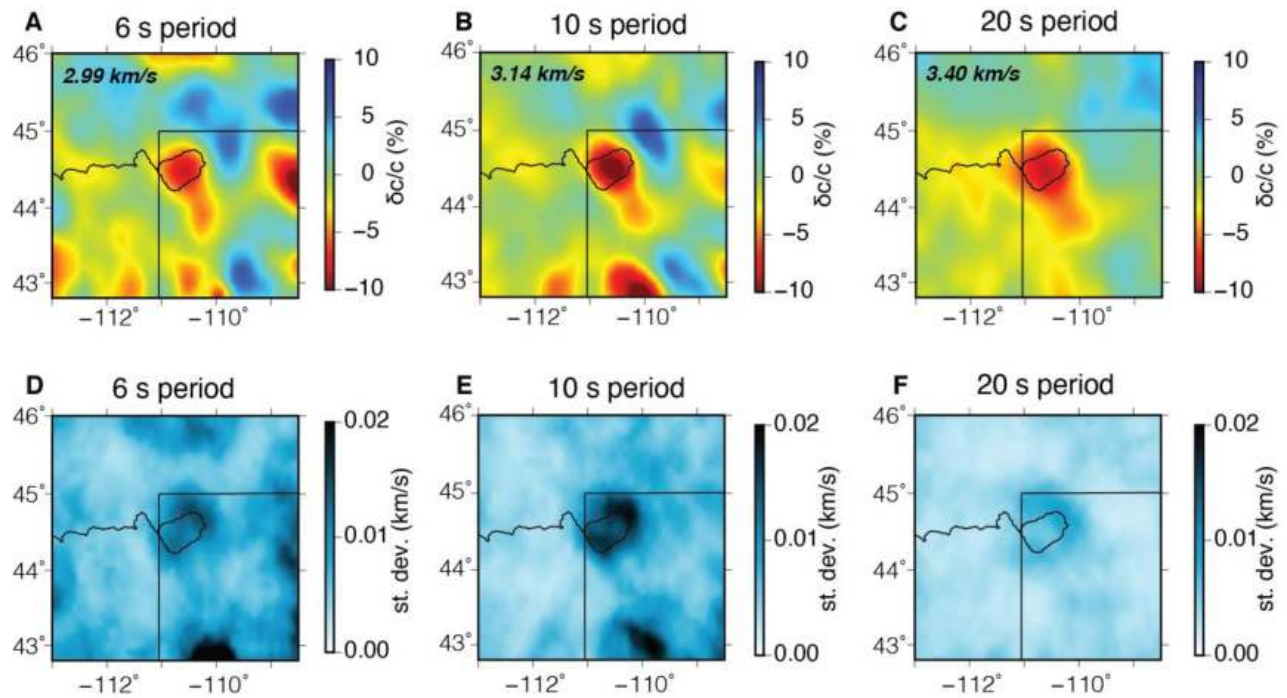
Figure S1.
Phase velocity inversion results for periods of 6, 10, and 20 s. The top row (panels A-C) shows the velocity perturbation with respect to the average Vs (shown in the top left of each map), and the bottom row (panels D-F) shows the standard deviation of the shear velocity in km/s. The black elliptical outline at the center of each panel marks the Yellowstone caldera.
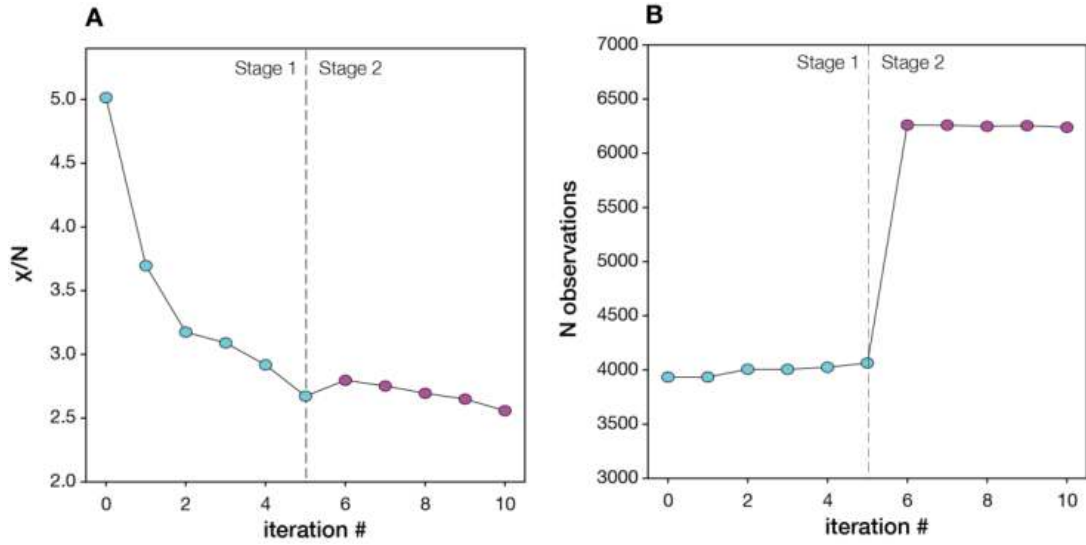
Figure S2
Misfit evolution during FWI. (A) Total misfit normalized by the number of observations for iterations 0 to 10. Stage 2 of the iteration, in which more virtual sources were added, started at iteration 6. (B) Total number of observations at each iteration.
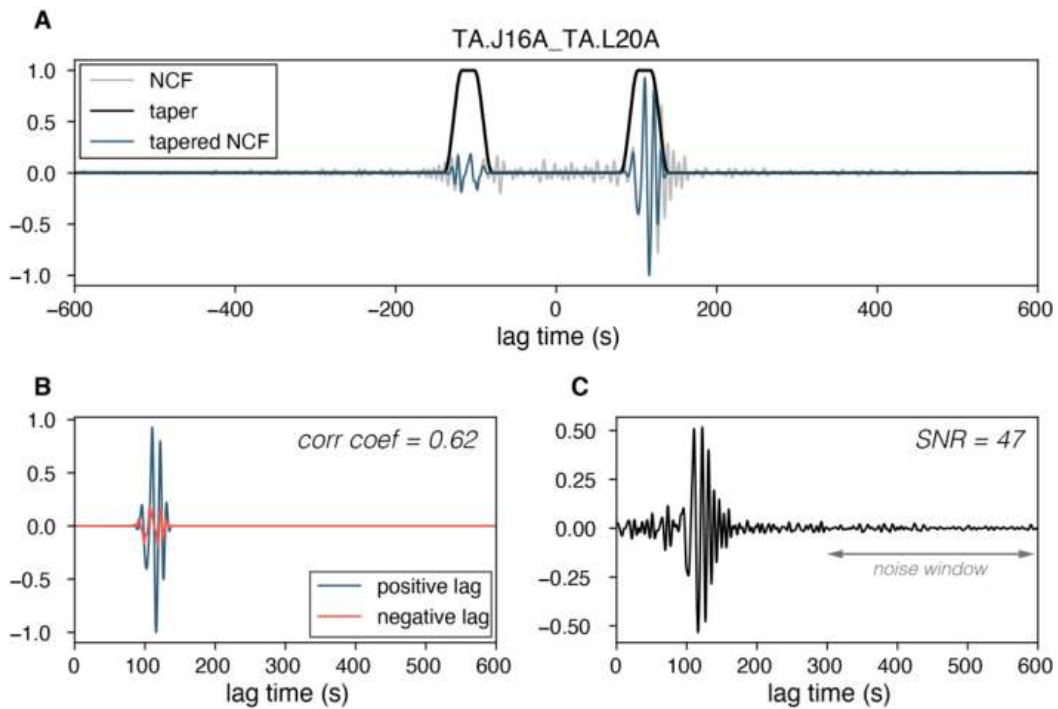
Figure S3.

Summary of steps used for data selection. (A) Noise correlation function between stations TA.J16A and TA.L20A. A cosine taper (black line) is applied to the raw waveform (gray line) to mute signal outside the surface wave window on both positive and negative lag times. (B) Positive (blue) and negative (orange) lag signals. The correlation coefficient between the two waveforms is shown in the upper right. (C) NCF after averaging the positive and negative lag signals (i.e., folding). The grey line shows the window used to calculate the RMS noise level, and the SNR is shown in the upper right.
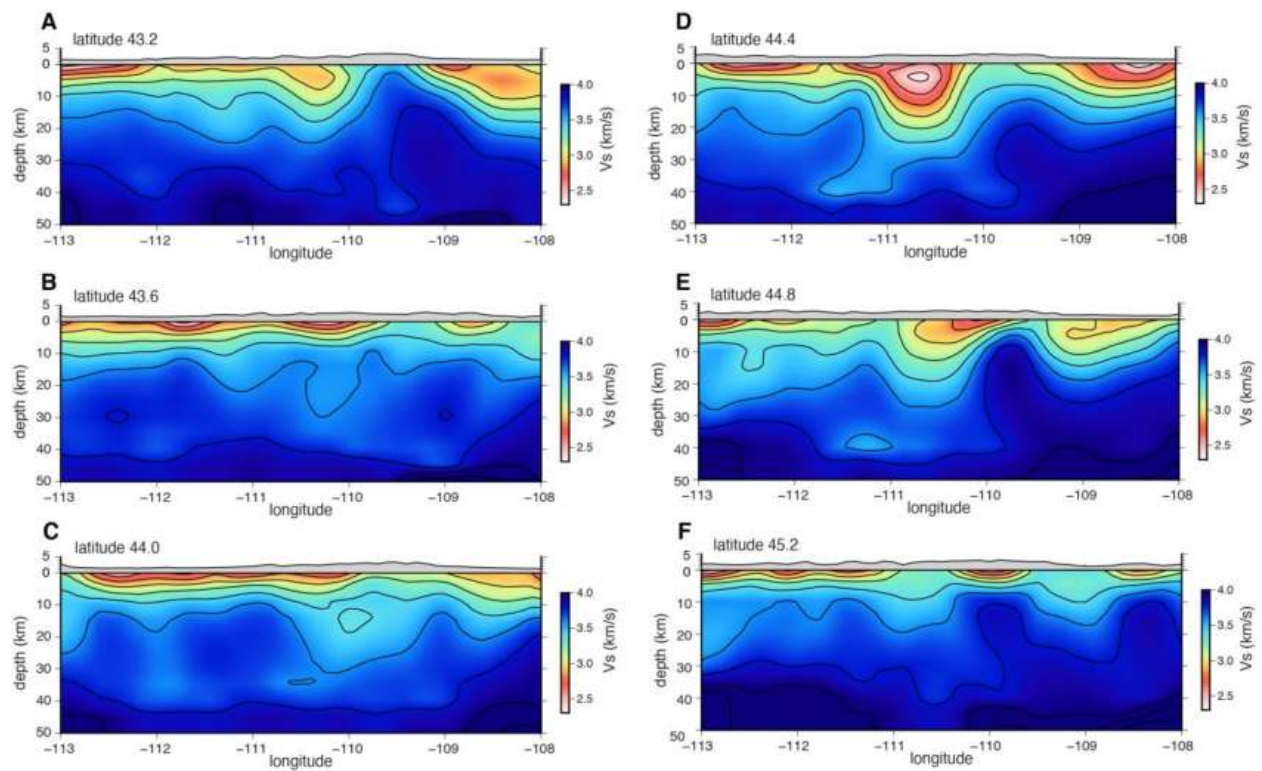
Figure S4.
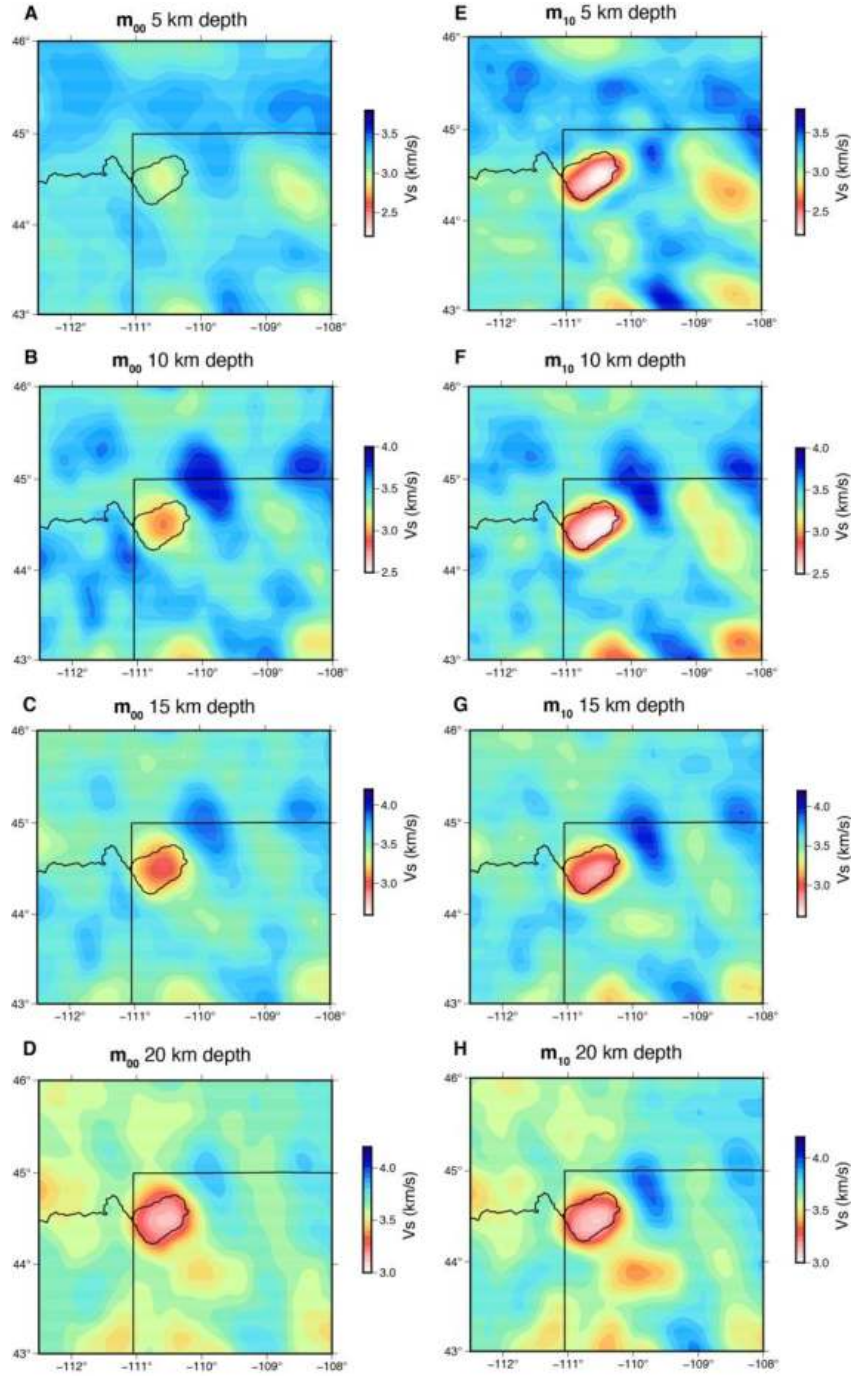Longitudinal slices of model $\mathbf{m_{10}}$ at six different latitudes ranging between 43.2º - 45.2º.

Figure S5.
V_S maps of models m_{00} (left column) and m_{10} (right column) at depths of 5, 10, 15, and 20 km.
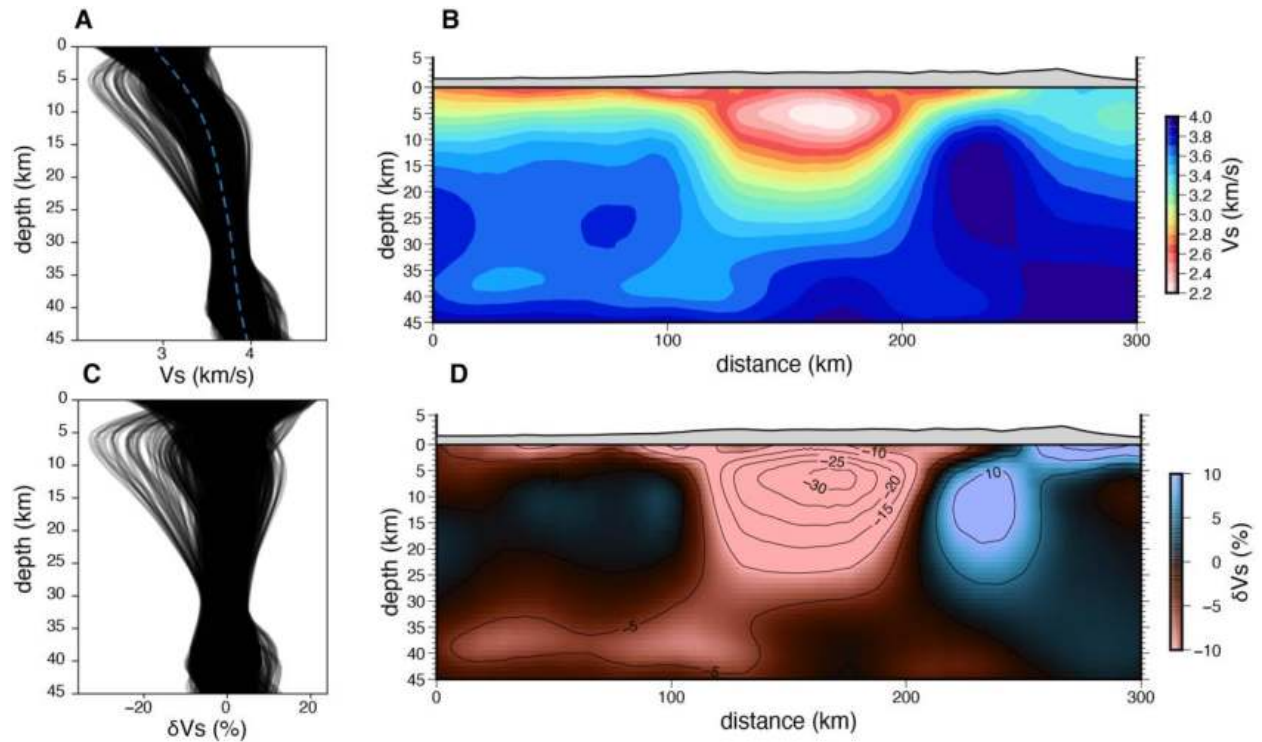
Figure S6. (A) Collection of all 1D V_S profiles of $\mathbf{m_{10}}$ (grid spacing of 0.1 x 0.1 degrees). The dashed blue line shows the average profile that was used to calculate velocity perturbations $\underline{\delta V_S}$. (B) V_S cross section along profile X-X' (same as shown in Figure 2B). (C) Same as A, but for 1D $\underline{\delta V_S}$ profiles. (D) $\underline{\delta V_S}$ cross section along same profile shown in B.
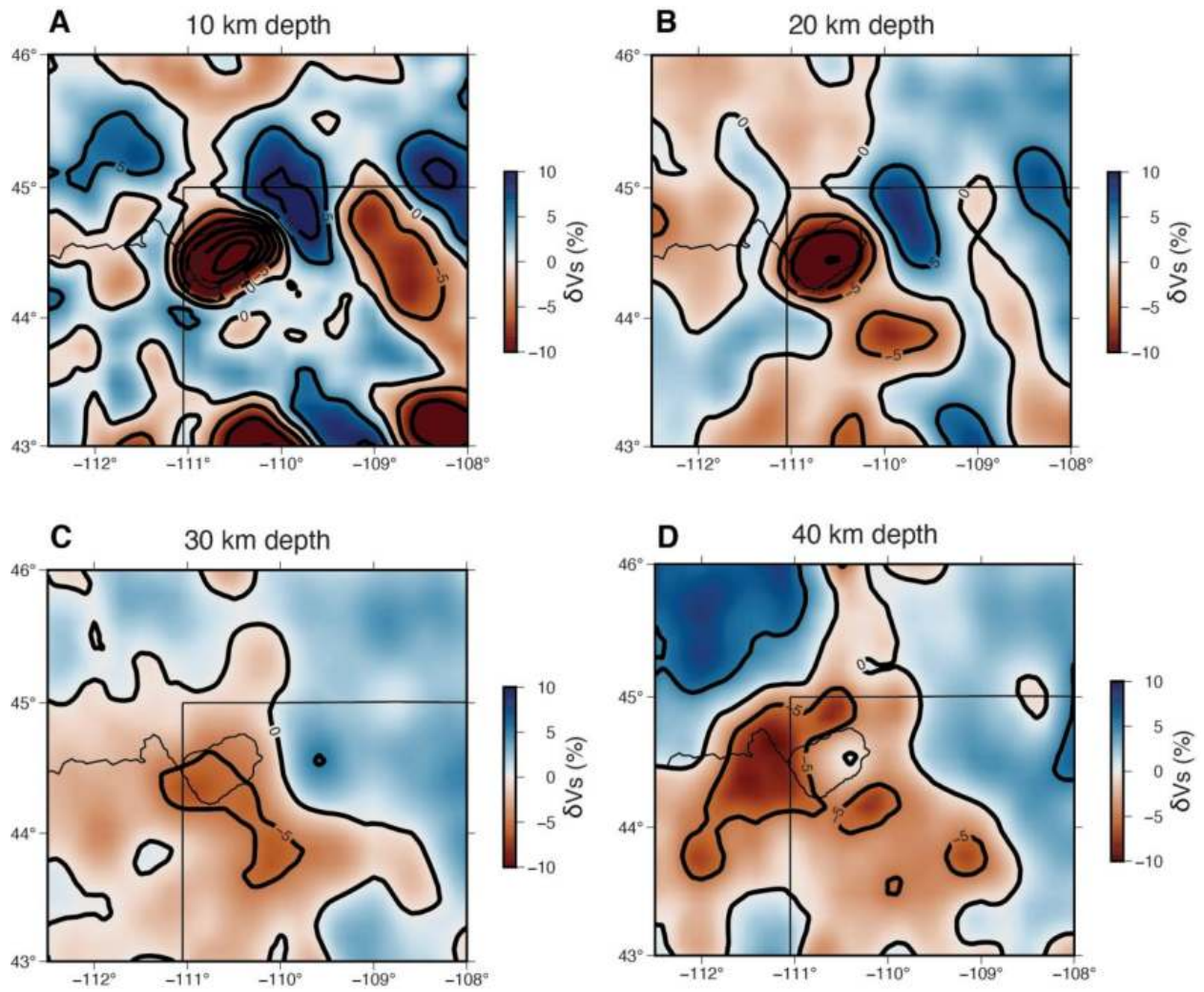
Figure S7. Relative velocity perturbations of model $\mathbf{m}_{10}$ at depths of 10, 20, 30, and 40 km.
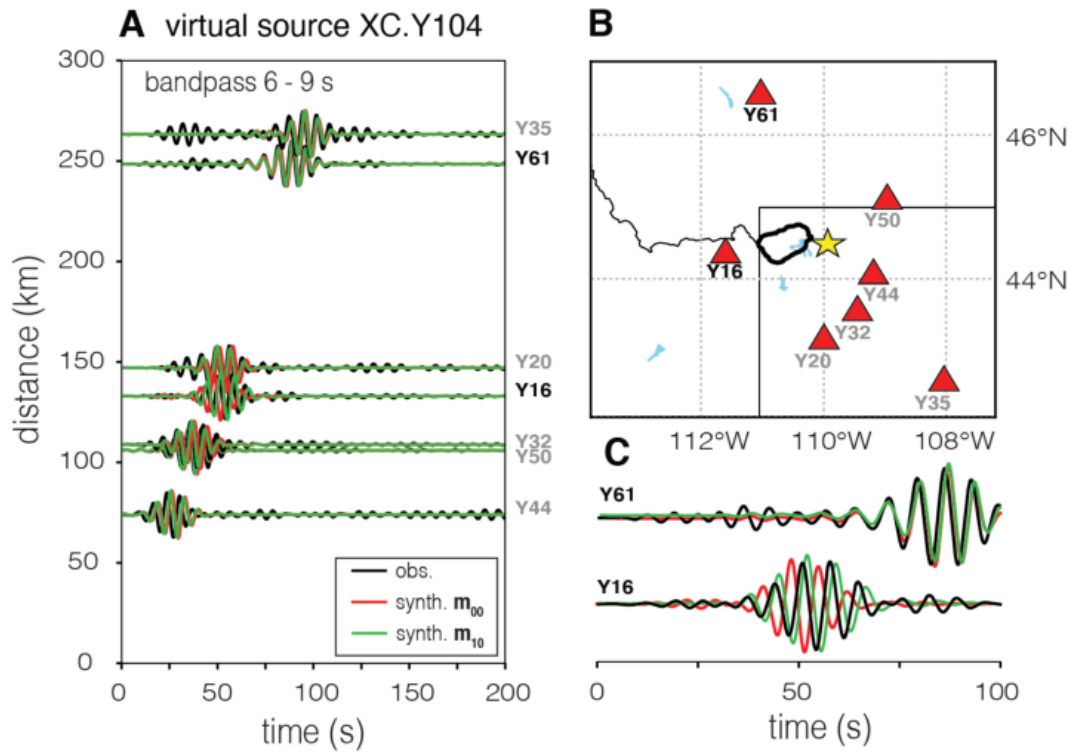
Figure S8.
(A) Record section of waveform fits from virtual source XC.Y104 (yellow star), filtered between 6 - 9 s, at stations shown in panel (B). (C) Close-up of waveform fits for stations XC.Y61 and XC.Y16. Observed data are shown in black and synthetics from the starting model and final model are shown in red and green, respectively.
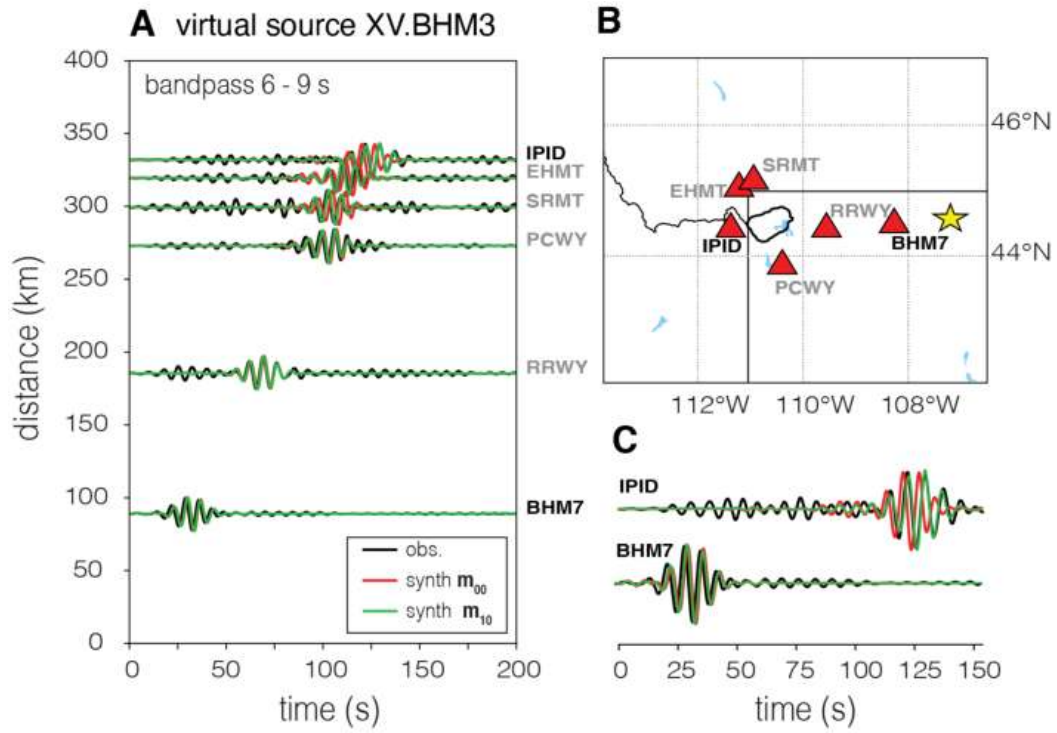
Figure S9.
Same as Fig. S6, but for a virtual source at station XV.BHM3 (yellow star). Virtual sources from the XV network were not used in the inversion.
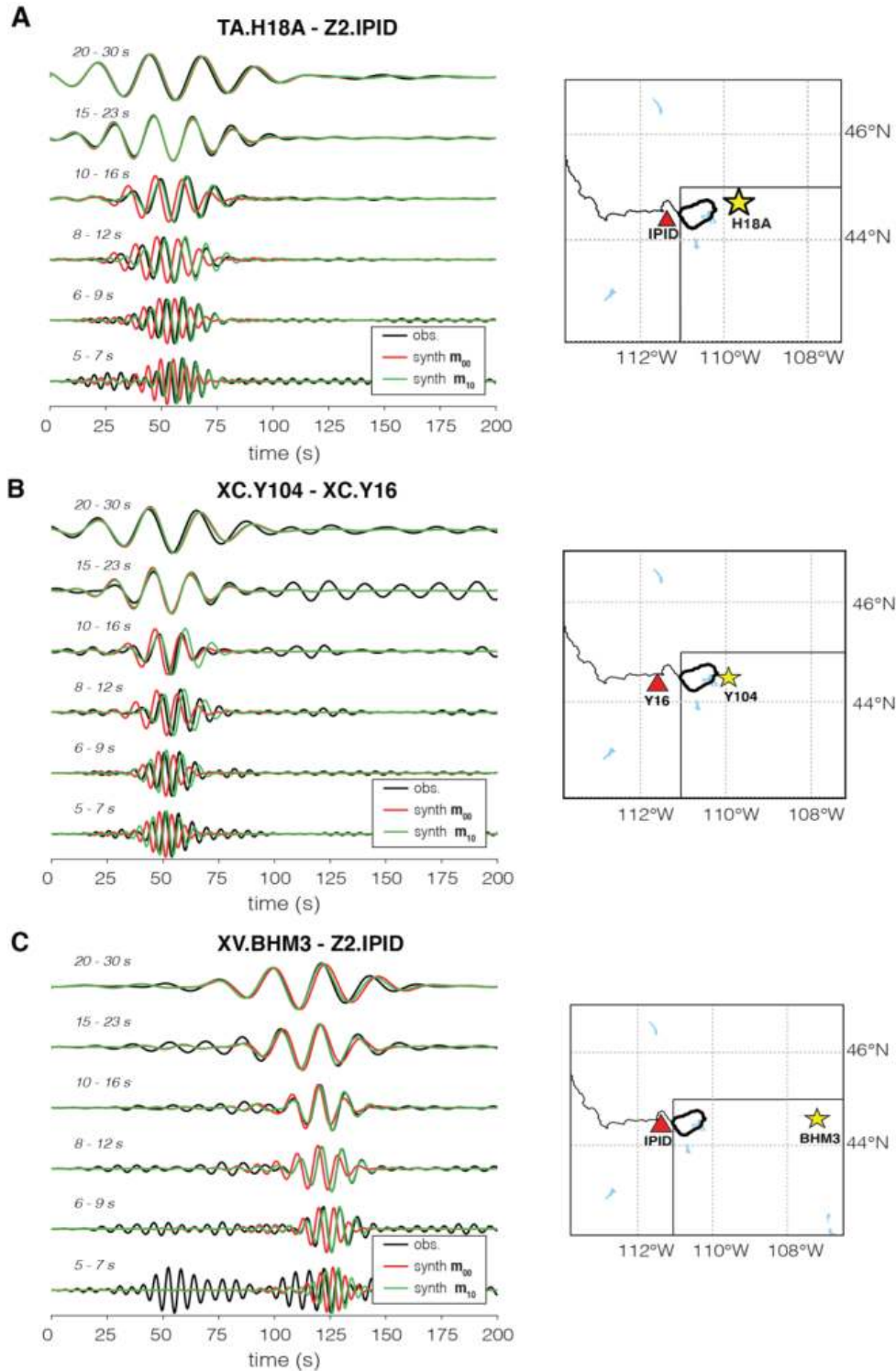
Figure S10.
Filter banks showing waveform fits for caldera traversing paths TA.H18A - Z2.IPID (panel A), XC.Y104 - XC.Y16 (panel B) and XV.BHM3 - Z2.IPID (panel V). The period range used in each bandpass filter is shown at the top left of the waveforms. Maps to the right of the filter banks show the location of the virtual source (yellow star) and station (red triangle). Data shown in panel C were not used in the inversion.
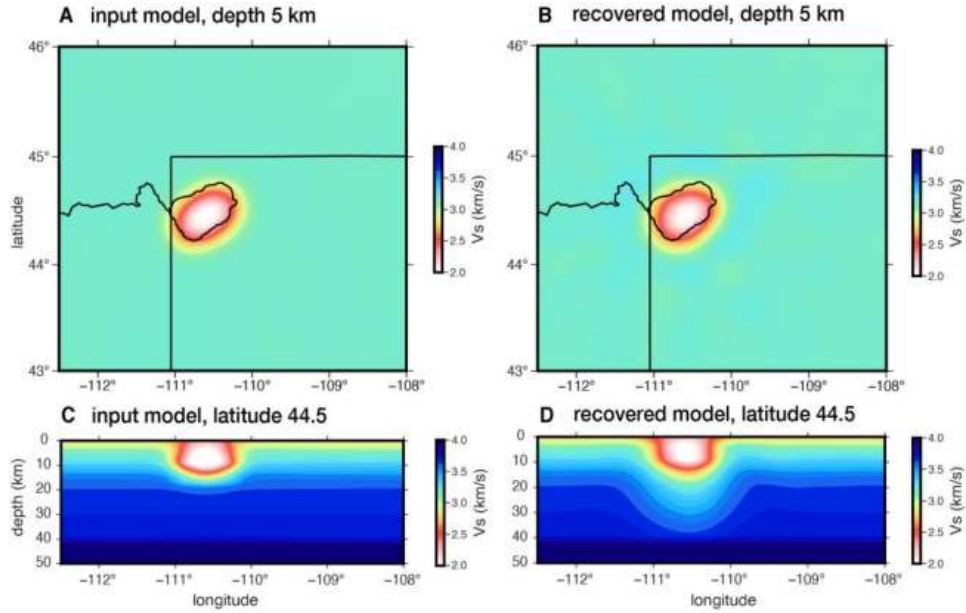
Figure S11.
Resolution test results. Top row: Maps of the input (A) and recovered (B) models, at a depth of 5 km. Bottom row: Vertical cross sections at a latitude of 44.5° of the input (C) and recovered (D) models.

Seismic Network	Network Code	Reference
Geodynamics of the Yellowstone Hotspot from Seismic and GPS imaging	XC	https://doi.org/10.7914/SN/XC_2000
Montana BB Array	XS	https://doi.org/10.7914/SN/XS_1999
USArray Transportable Array	TA	https://doi.org/10.7914/SN/TA
Bighorn Arch Seismic Experiment	XV	https://doi.org/10.7914/SN/XV_2009
Noise Observatory for Imaging the Subsurface beneath Yellowstone	Z2	Seats & Lawrence (2004)
Yellowstone National Park Seismograph Network	WY	https://doi.org/10.7914/SN/WY
Intermountain West Seismic Network	IW	https://doi.org/10.7914/SN/IW
United States National Seismic Network	US	https://doi.org/10.7914/SN/US

Table S1. Seismic networks used in this study.

Oxide	Weight %
SiO_2	75.5
Al_2O_3	12.6
FeO	0.3
CaO	0.3
Na_2O	3.4
K_2O	5.2

Table S2. Composition of granitoid used to calculate seismic velocity, in terms of 6 major oxide components. The composition is representative of the Lava Creek Tuff (*50*).

References and Notes

1. R. L. Christiansen, J. B. Lowenstern, R. B. Smith, H. Heasler, L. A. Morgan, M. Nathenson, L. G. Mastin, L. J. P. Muffler, E. Robinson, *Preliminary Assessment of Volcanic and Hydrothermal Hazards in Yellowstone National Park and Vicinity* (US Geological Survey, 2007).

2. C. J. Wilson, G. F. Cooper, K. J. Chamberlain, S. J. Barker, M. L. Myers, F. Illsley-Kemp, J. Farrell, No single model for supersized eruptions and their magma bodies. *Nat. Rev. Earth Environ.* **2**, 610–627 (2021).

3. S. Self, The effects and consequences of very large explosive volcanic eruptions. *Philos. Trans. A Math. Phys. Eng. Sci.* **364**, 2073–2097 (2006).

4. M. T. Jones, R. S. J. Sparks, P. J. Valdes, The climatic impact of supervolcanic ash blankets. *Clim. Dyn.* **29**, 553–564 (2007).

5. N. E. Matthews, J. A. Vazquez, A. T. Calvert, Age of the Lava Creek supereruption and magma chamber assembly at Yellowstone based on 40 Ar/39 Ar and U-P b dating of sanidine and zircon crystals. *Geochem. Geophys. Geosyst.* **16**, 2508–2528 (2015).

6. J. B. Lowenstern, S. Hurwitz, Monitoring a supervolcano in repose: Heat and volatile flux at the Yellowstone Caldera. *Elements (Quebec)* **4**, 35–40 (2008).

7. W. L. Chang, R. B. Smith, J. Farrell, C. M. Puskas, An extraordinary episode of Yellowstone caldera uplift, 2004–2010, from GPS and InSAR observations. *Geophys. Res. Lett.* **37**, n/a (2010).

8. M. E. Stelten, K. M. Cooper, J. A. Vazquez, A. T. Calvert, J. J. Glessner, Mechanisms and timescales of generating eruptible rhyolitic magmas at Yellowstone caldera from zircon and sanidine geochronology and geochemistry. *J. Petrol.* **56**, 1607–1642 (2015).

9. J. F. Wotzlaw, I. N. Bindeman, R. A. Stern, F. X. D'Abzac, U. Schaltegger, Rapid heterogeneous assembly of multiple magma reservoirs prior to Yellowstone supereruptions. *Sci. Rep.* **5**, 14026 (2015).

10. A. E. Rubin, K. M. Cooper, C. B. Till, A. J. R. Kent, F. Costa, M. Bose, D. Gravley, C. Deering, J. Cole, Rapid cooling and cold storage in a silicic magma reservoir recorded in individual crystals. *Science* **356**, 1154–1156 (2017).

11. S. Husen, R. B. Smith, G. P. Waite, Evidence for gas and magmatic sources beneath the Yellowstone volcanic field from seismic tomographic imaging. *J. Volcanol. Geotherm. Res.* **131**, 397–410 (2004).

12. J. C. Stachnik, K. Dueker, D. L. Schutt, H. Yuan, Imaging Yellowstone plume-lithosphere interactions from inversion of ballistic and diffusive Rayleigh wave dispersion and crustal thickness data. *Geochem. Geophys. Geosyst.* 10.1029/2008GC001992 (2008).

13. J. Farrell, R. B. Smith, S. Husen, T. Diehl, Tomography from 26 years of seismicity revealing that the spatial extent of the Yellowstone crustal magma reservoir extends well beyond the Yellowstone caldera. *Geophys. Res. Lett.* **41**, 3068–3073 (2014).

14. H. H. Huang, F. C. Lin, B. Schmandt, J. Farrell, R. B. Smith, V. C. Tsai, Volcanology. The Yellowstone magmatic system from the mantle plume to the upper crust. *Science* **348**, 773–776 (2015).

15. C. Jiang, B. Schmandt, J. Farrell, F. C. Lin, K. M. Ward, Seismically anisotropic magma reservoirs underlying silicic calderas. *Geology* **46**, 727–730 (2018).

16. R. Chu, D. V. Helmberger, D. Sun, J. M. Jackson, L. Zhu, Mushy magma beneath Yellowstone. *Geophys. Res. Lett.* **37**, n/a (2010).

17. G. Nolet, F. A. Dahlen, Wave front healing and the evolution of seismic delay times. *J. Geophys. Res.* **105** (B8), 19043–19054 (2000).

18. R. Maguire, B. Schmandt, M. Chen, C. Jiang, J. Li, J. Wilgus, Resolving continental magma reservoirs with 3D surface wave tomography. *Geochem. Geophys. Geosyst.* **23**, (2022).

19. C. Tape, Q. Liu, A. Maggi, J. Tromp, Adjoint tomography of the southern California crust. *Science* **325**, 988–992 (2009).

20. M. Chen, H. Huang, H. Yao, R. van der Hilst, F. Niu, Low wave speed zones in the crust beneath SE Tibet revealed by ambient noise adjoint tomography. *Geophys. Res. Lett.* **41**, 334–340 (2014).

21. A. F. Flinders, D. R. Shelly, P. B. Dawson, D. P. Hill, B. Tripoli, Y. Shen, Seismic evidence for significant melt beneath the Long Valley Caldera, California, USA. *Geology* **46**, 799–802 (2018).

22. Materials and methods are available as supplementary materials.

23. H. I. Shamloo, C. B. Till, Decadal transition from quiescence to supereruption: Petrologic investigation of the Lava Creek Tuff, Yellowstone Caldera, WY. *Contrib. Mineral. Petrol.* **174**, 32 (2019).

24. K. S. Befus, J. E. Gardner, Magma storage and evolution of the most recent effusive and explosive eruptions from Yellowstone Caldera. *Contrib. Mineral. Petrol.* **171**, 30 (2016).

25. J. G. Berryman, Long-wavelength propagation in composite elastic media II. Ellipsoidal inclusions. *J. Acoust. Soc. Am.* **68**, 1820–1831 (1980).

26. M. B. Holness, Melt–solid dihedral angles of common minerals in natural rocks. *J. Petrol.* **47**, 791–800 (2005).

27. Y. Takei, Effect of pore geometry on VP/VS: From equilibrium geometry to crack. *J. Geophys. Res. Solid Earth* **107**, ECV-6 (2002).

28. K. V. Cashman, G. Giordano, Calderas and magma reservoirs. *J. Volcanol. Geotherm. Res.* **288**, 28–45 (2014).

29. L. Caricchi, L. Burlini, P. Ulmer, Propagation of P and S-waves in magmas with different crystal contents: Insights into the crystallinity of magmatic reservoirs. *J. Volcanol. Geotherm. Res.* **178**, 740–750 (2008).

30. B. Liu, C. T. Lee, Fast melt expulsion from crystal-rich mushes via induced anisotropic permeability. *Earth Planet. Sci. Lett.* **571**, 117113 (2021).

31. G. W. Bergantz, J. M. Schleicher, A. Burgisser, On the kinematics and dynamics of crystal-rich systems. *J. Geophys. Res. Solid Earth* **122**, 6131–6159 (2017).

32. M. Beyreuther, R. Barsch, L. Krischer, T. Megies, Y. Behr, J. Wassermann, ObsPy: A Python toolbox for seismology. *Seismol. Res. Lett.* **81**, 530–533 (2010).

33. K. J. Seats, J. F. Lawrence, The seismic structure beneath the Yellowstone Volcano Field from ambient seismic noise. *Geophys. Res. Lett.* **41**, 8277–8282 (2014).

34. G. D. Bensen, M. H. Ritzwoller, M. P. Barmin, A. L. Levshin, F. Lin, M. P. Moschetti, N. M. Shapiro, Y. Yang, Processing seismic ambient noise data to obtain reliable broad-band surface wave dispersion measurements. *Geophys. J. Int.* **169**, 1239–1260 (2007).

35. K. G. Sabra, P. Gerstoft, P. Roux, W. A. Kuperman, M. C. Fehler, Extracting time-domain Green's function estimates from ambient seismic noise. *Geophys. Res. Lett.* **32**, L03310 (2005).

36. N. M. Shapiro, M. Campillo, L. Stehly, M. H. Ritzwoller, High-resolution surface-wave tomography from ambient seismic noise. *Science* **307**, 1615–1618 (2005).

37. H. Fang, R. D. Van Der Hilst, M. V. de Hoop, K. Kothari, S. Gupta, I. Dokmanić, Parsimonious seismic tomography with Poisson Voronoi projections: Methodology and validation. *Seismol. Res. Lett.* **91**, 343–355 (2020).

38. M. C. White, H. Fang, N. Nakata, Y. Ben-Zion, PyKonal: A Python package for solving the eikonal equation in spherical and Cartesian coordinates using the fast marching method. *Seismol. Res. Lett.* **91**, 2378–2389 (2020).

39. B. Schmandt, F. C. Lin, K. E. Karlstrom, Distinct crustal isostasy trends east and west of the Rocky Mountain Front. *Geophys. Res. Lett.* **42**, 10–290 (2015).

40. K. Mosegaard, A. Tarantola, Monte Carlo sampling of solutions to inverse problems. *J. Geophys. Res.* **100**, 12431–12447 (1995).

41. R. B. Herrmann, Computer programs in seismology: An evolving tool for instruction and research. *Seismol. Res. Lett.* **84**, 1081–1088 (2013).

42. A. Fichtner, Full seismic waveform modelling and inversion. Springer Science & Business Media. (2010).

43. J. Tromp, C. Tape, Q. Liu, Seismic tomography, adjoint methods, time reversal and banana-doughnut kernels. *Geophys. J. Int.* **160**, 195–216 (2005).

44. J. Tromp, D. Komatitsch, Q. Liu, Spectral-element and adjoint methods in seismology. *Commun. Comput. Phys.* **3**, 1–32 (2008).

45. N. I. Christensen, W. D. Mooney, Seismic velocity structure and composition of the continental crust: A global view. *J. Geophys. Res.* **100** (B6), 9761–9788 (1995).

46. Y. Liu, F. Niu, M. Chen, W. Yang, 3-D crustal and uppermost mantle structure beneath NE China revealed by ambient noise adjoint tomography. *Earth Planet. Sci. Lett.* **461**, 20–29 (2017).

47. K. Ueki, H. Iwamori, Density and seismic velocity of hydrous melts under crustal and upper mantle conditions. *Geochem. Geophys. Geosyst.* **17**, 1799–1814 (2016).

48. M. Paulatto, M. Moorkamp, S. Hautmann, E. Hooft, J. V. Morgan, R. S. J. Sparks, Vertically extensive magma reservoir revealed from joint inversion and quantitative interpretation of seismic and gravity data. *J. Geophys. Res. Solid Earth* **124**, 11170–11191 (2019).

49. F. Gassmann, Elastic waves through a packing of spheres. *Geophysics* **16**, 673–685 (1951).

50. R. L. Christiansen, *The Quaternary and Pliocene Yellowstone Plateau Volcanic Field of Wyoming, Idaho, and Montana*, vol. 729 (US Department of the Interior, US Geological Survey, 2001).